A New Form of the Biot-Savart Law and Decomposition of Vector Magnetograms

Viacheslav Titov[1], Cooper Downs[1], Tibor Torok[1], Jon Linker[1], Michael Prazak[2], and Jiong Qiu[2]

[1]Predictive Science Inc., San Diego, USA
[2]Montana State University, Department of Physics, Bozeman, USA

April 16, 2024

A New Form of the Biot-Savart Law and Decomposition of Vector Magnetograms

Viacheslav Titov[1], Cooper Downs[1], Tibor Torok[1], Jon Linker[1], Michael Prazak[2], and Jiong Qiu[2]

[1]Predictive Science Inc., San Diego, USA,
[2]Montana State University, Department of Physics, Bozeman, USA

PRESENTED AT:

AGU23 WIDE. OPEN. SCIENCE.

1. INTRODUCTION

We have derived a new form of the Biot-Savart law (BSL) that allows one to calculate the coronal magnetic field generated by a given closed line current or current density field under the condition that its radial magnetic component vanishes at the photospheric boundary.

Thus, the superposition of this BSL field and the potential magnetic field determined, say, from an observed distribution of the photospheric radial magnetic field provides the total current-carrying magnetic field that matches this distribution.

This representation of the coronal magnetic field is useful for solving the following two problems:

1. Modeling of pre-eruptive configurations (PEC) that are superposed of the magnetic flux rope (MFR) field and potential magnetic field, where the MFR is modeled by using our requlatized Biot-Savart laws (RBSLs, see Titov et al. (2018) (https://iopscience.iop.org/article/10.3847/2041-8213/aaa3da) and Titov et al. (2021) (https://iopscience.iop.org/article/10.3847/1538-4365/abfe0f));
2. Decomposition of the photospheric vector magnetic data into three components: potential field and the fields generated by subphotospheric and coronal currents.

The solution of the second problem can actually be helpful for solving the first one, as it allows one to reveal the location of MFRs and pariticularly their footprints, which can greatly enhance the power and accuracy of the RBSL method.

Our field decomposition is similar to the Gaussian decomposition of the magnetic field that was recently described by Schuck et al. (2022) (https://iopscience.iop.org/article/10.3847/1538-4357/ac739a). However, there is a significant difference between these two decompositions. In contrast to Schuck et al. (2022) (https://iopscience.iop.org/article/10.3847/1538-4357/ac739a), our decomposition implies that the field generated by coronal currents has a vanishing radial component at the photospheric boundary. We achieve this by deriving and using a modified form of the BSL that automatically satisfies this boundary condition. As it does not change the radial magnetic component at the boundary, we call this BSL ***magnetogram-matching***.

We apply this magnetogram-matching BSL to the sub-photospheric currents that provide a closure to the coronal current loops. We show that the field generated by these currents actually coincides with the so-called toroidal magnetic field, which is due to the currents piercing the photospheric boundary in the Gaussian decomposition (see Schuck et al. (2022) (https://iopscience.iop.org/article/10.3847/1538-4357/ac739a)).

We demonstrate that our method of decomposition of the photospheric magnetic data indeed allows one to identify the MFR footprints as well as its shape in projection to the photospheric surface, which both have to be very important constraints for a comprehensive modeling of PECs.

2. MAGNETOGRAM-MATCHING BIOT-SAVART LAW

Consider a line current of strength I flowing along a closed path $C \cup C^*$, where C and C^* are its parts above and below, respectively, the solar surface of radius $R_\odot$ (Figure 1). Let this path be represented by the radius- vector $\boldsymbol{R}(l)$ and parametrized by the arc length l measured from one of the foot point, so that $\boldsymbol{R}' = \mathrm{d}\boldsymbol{R}/\mathrm{d}l$ is a unit vector tangential to the path. Then, according to classical Biot-Savart law, the infinitesimal contribution of a path element of length $\mathrm{d}l$ to the magnetic field $\boldsymbol{B}_I$ produced by current I at a given point $\boldsymbol{x}$ is described by

$$\left[\frac{\mu I}{4\pi R_\odot}\right] \qquad \mathrm{d}\boldsymbol{B}_I = -\frac{(\boldsymbol{x}-\boldsymbol{\mathcal{R}})\times\boldsymbol{\mathcal{R}}'}{|\boldsymbol{x}-\boldsymbol{\mathcal{R}}|^3}\mathrm{d}l = \frac{\boldsymbol{r}\times\mathrm{d}\boldsymbol{r}}{r^3} = \frac{\hat{\boldsymbol{r}}\times\mathrm{d}\boldsymbol{r}}{r^2}\,,$$
$$\boldsymbol{r} = \boldsymbol{x}-\boldsymbol{\mathcal{R}}\,, \quad \hat{\boldsymbol{r}} = \boldsymbol{r}/r\,,$$

where the expression in the brackets on the left hand side represents the unit in which $\boldsymbol{B}_I$ is measured. Similar expressions in the brackets will be used further for designating the units of other values in our poster. Also we assume hereafter that l and the lengths of all vectors are for simplicity normalized to the solar radius $R_\odot$.

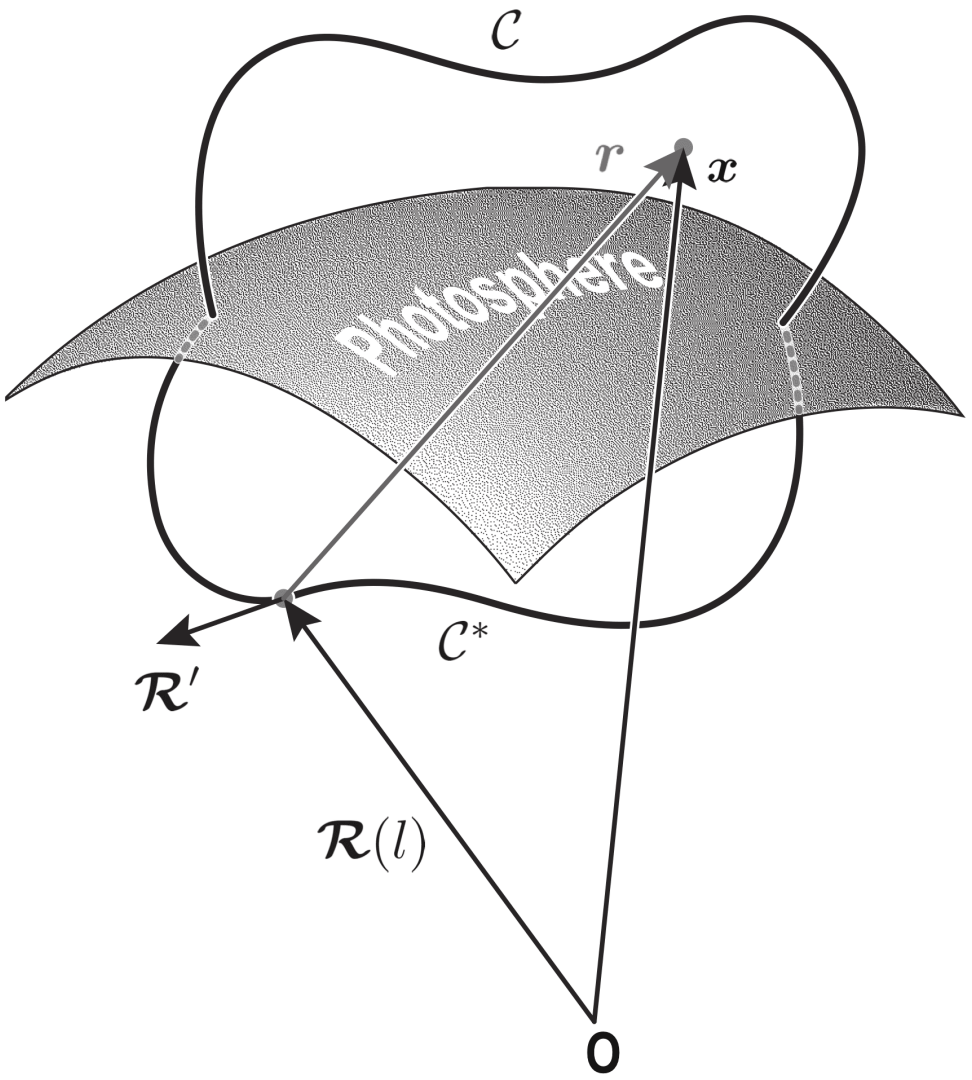

Figure 1. The radius-vector $\mathcal{R}(l)$ with the starting point at the center of the Sun 0 defines a line current path that consists of coronal and sub-photospheric parts, $\mathcal{C}$ and $\mathcal{C}^*$, respectively. The integration of the elementary Biot-Savart field along this path provides the magnetic field generated by the current circuit at a given point $\boldsymbol{x}$.

The result of integration of $d\boldsymbol{B}_I$ along the path is a potential magnetic field that for $r > a/R_\odot$ approximately describes the field of a magnetic flux rope (MFR) with a circular cross-section of radius a (Titov et al. 2018 (https://iopscience.iop.org/article/10.3847/2041-8213/aaa3da)). This field generally has a non-vanishing radial component at the photospheric boundary.

It turns out that, for every elementary field $d\boldsymbol{B}_I$, there exists a corresponding potential magnetic field whose sources are located at $|\boldsymbol{x}| \le 1$ and whose radial component at the boundary equals the radial component of $-d\boldsymbol{B}_I$. We call this potential field as the compensating one and denote it as $d\boldsymbol{B}_C$ or $d\boldsymbol{B}_{C*}$ depending on whether the corresponding current element belongs to the path C or C^*, respectively.

We have proved that these compensating fields have the following expressions:

$$\left[\frac{\mu I}{4\pi R_\odot}\right] \qquad \mathrm{d}\boldsymbol{B}_{\mathcal{C}} = -\frac{\hat{\boldsymbol{r}}_* \times \mathrm{d}\boldsymbol{r}}{\mathcal{R} r_*^2} + \frac{(\hat{\boldsymbol{r}}_* \cdot \mathrm{d}\boldsymbol{r})\ \hat{\boldsymbol{r}}_* \times \hat{\boldsymbol{x}}}{\mathcal{R}\, r_*^2\ (\hat{\boldsymbol{r}}_* \cdot \hat{\boldsymbol{x}} + 1)}$$
$$+ \left(\frac{1}{r_*} + \frac{1}{|\boldsymbol{x}|}\right) \frac{[(\hat{\boldsymbol{r}}_* + \hat{\boldsymbol{x}}) \times (\hat{\boldsymbol{r}}_* \times \mathrm{d}\boldsymbol{r})] \times \hat{\boldsymbol{x}}}{\mathcal{R}\, r_*\ (\hat{\boldsymbol{r}}_* \cdot \hat{\boldsymbol{x}} + 1)^2}\,,$$

$$\left[\frac{\mu I}{4\pi R_\odot}\right] \qquad \mathrm{d}\boldsymbol{B}_{\mathcal{C}^*} = -\frac{\hat{\boldsymbol{r}} \times \mathrm{d}\boldsymbol{r}}{r^2} + \frac{(\hat{\boldsymbol{r}} \cdot \mathrm{d}\boldsymbol{r})\ \hat{\boldsymbol{r}} \times \hat{\boldsymbol{x}}}{r^2\ (\hat{\boldsymbol{r}} \cdot \hat{\boldsymbol{x}} + 1)}$$
$$+ \left(\frac{1}{r} + \frac{1}{|\boldsymbol{x}|}\right) \frac{[(\hat{\boldsymbol{r}} + \hat{\boldsymbol{x}}) \times (\hat{\boldsymbol{r}} \times \mathrm{d}\boldsymbol{r})] \times \hat{\boldsymbol{x}}}{r\ (\hat{\boldsymbol{r}} \cdot \hat{\boldsymbol{x}} + 1)^2}\,,$$

where

$$\boldsymbol{\mathcal{R}}_* = \boldsymbol{\mathcal{R}}/\mathcal{R}^2\,,$$
$$\boldsymbol{r}_* = \boldsymbol{x} - \boldsymbol{\mathcal{R}}_*\,, \quad \hat{\boldsymbol{r}}_* = \boldsymbol{r}_*/r_*\,,$$
$$\hat{\boldsymbol{x}} = \boldsymbol{x}/|\boldsymbol{x}|\,.$$

In addition, we have proved that $\mathrm{d}\boldsymbol{B}_I$+$\mathrm{d}\boldsymbol{B}_{C^*}$ can be integrated analytically, so that the resulting magnetogram-matching BSL for the whole circuit acquires the following form:

$$\boldsymbol{B}_{I\ominus} = \int_{\mathcal{C}} (\mathrm{d}\boldsymbol{B}_I + \mathrm{d}\boldsymbol{B}_{\mathcal{C}}) + \boldsymbol{\Theta}(\boldsymbol{x}, \boldsymbol{r})\Big|_{\boldsymbol{r}=\boldsymbol{x}-\boldsymbol{\mathcal{R}}_1}^{\boldsymbol{r}=\boldsymbol{x}-\boldsymbol{\mathcal{R}}_2}$$

where

$$\boldsymbol{\Theta}(\boldsymbol{x}, \boldsymbol{r}) = \left(\frac{1}{r} + \frac{1}{|\boldsymbol{x}|}\right) \frac{\hat{\boldsymbol{r}} \times \hat{\boldsymbol{x}}}{\hat{\boldsymbol{r}} \cdot \hat{\boldsymbol{x}} + 1}\,.$$

The latter term describes the field generated by the current at the subphotospheric path C^* with the end points $\mathcal{R}_1$ and $\mathcal{R}_2$ under the condition that its radial component vanishes at the boundary. In fact, the resulting solenoidal field is toroidal, since it has no radial component everywhere in the coronal volume.

Figure 2 illustrates the field line structure obtained with the magnetogram-matching BSL for a particular coronal current path.

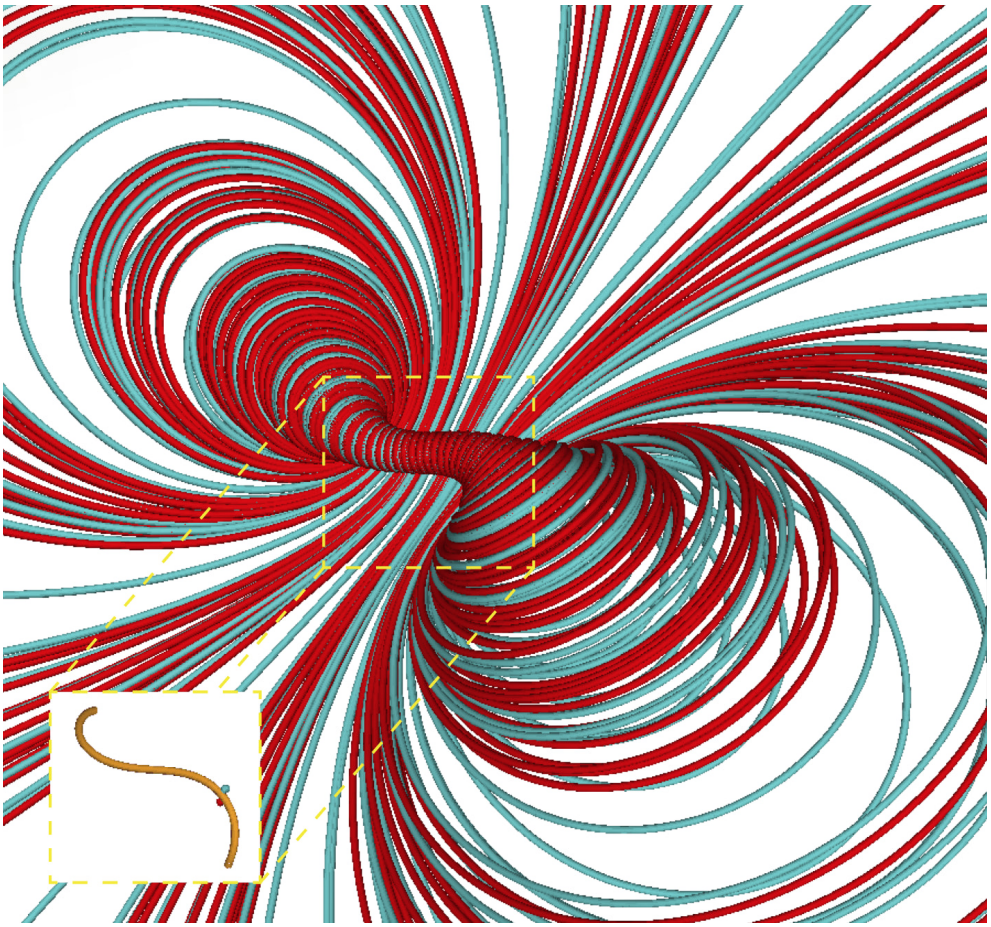

Figure 2. Top view of magnetic field lines for the configuration defined by the magnetogram-matching Biot-Savart law; the inset shows the corresponding current path $\mathcal{C}$ (orange) and two arbitrary starting points (close to the path) for the plotted field lines.

We have generalized this BSL for the current distributed in the coronal volume V and at the boundary S with the density $\mathbf{J}$. The resulting expression has the following form:

$$\left[\frac{\mu I}{4\pi R_\odot}\right] \quad \boldsymbol{B}_{I\ominus} = \int_V \mathrm{d}V \left[\frac{\boldsymbol{J}\times\hat{\boldsymbol{r}}}{r^2} + \frac{\hat{\boldsymbol{r}}_*\times\boldsymbol{J}}{Rr_*^2} - \frac{(\hat{\boldsymbol{r}}_*\cdot\boldsymbol{J})\,\hat{\boldsymbol{r}}_*\times\hat{\boldsymbol{x}}}{R\,r_*^2\,(\hat{\boldsymbol{r}}_*\cdot\hat{\boldsymbol{x}}+1)} - \left(\frac{1}{r_*}+\frac{1}{|\boldsymbol{x}|}\right)\frac{[(\hat{\boldsymbol{r}}_*+\hat{\boldsymbol{x}})\times(\hat{\boldsymbol{r}}_*\times\boldsymbol{J})]\times\hat{\boldsymbol{x}}}{R\,r_*\,(\hat{\boldsymbol{r}}_*\cdot\hat{\boldsymbol{x}}+1)^2}\right] - \int_S \mathrm{d}S\left(\frac{1}{r}+\frac{1}{|\boldsymbol{x}|}\right)\frac{\left(\boldsymbol{J}\cdot\hat{\boldsymbol{R}}\right)\hat{\boldsymbol{r}}\times\hat{\boldsymbol{x}}}{\hat{\boldsymbol{r}}\cdot\hat{\boldsymbol{x}}+1},$$

where the integrals over the volume and the surface describe the coronal and toroidal fields, respectively.

In addition, we have derived the following explicit expression for the toroidal vector potential:

$$\left[\frac{\mu I}{4\pi}\right] \qquad \boldsymbol{A}_T = f(\boldsymbol{x})\,\hat{\boldsymbol{x}}\,,$$

$$f(\boldsymbol{x}) = \int_S \mathrm{d}S\,\left(\boldsymbol{J}\cdot\hat{\boldsymbol{R}}\right) G_f\,,$$

$$G_f = -\ln\left(\boldsymbol{x}\cdot\boldsymbol{r} + |\boldsymbol{x}|r\right)\,,$$

where $f(\mathbf{x})$ is the toroidal-field flux function (TFFF) and G_f is the corresponding Green's function.

3. DECOMPOSITION OF VECTOR MAGNETOGRAMS

Consider coronal magnetic configurations whose current resides only in closed loops that are rooted in the photospheric boundary. This is likely a generic case for the solar active regions. The theory presented above then suggests that the magnetic field in this case can be decomposed into three components: (1) the toroidal magnetic field produced by subphotospheric closure currents, (2) the magnetic field generated by coronal current loops under the condition that their radial magnetic component vanishes at the boundary, and (3) the potential magnetic field whose radial component at the photospheric boundary is generated by subphotospheric currents that do not reach the boundary.

Application of this decomposition to the photospheric magnetic field reveals the individual contributions of these three current systems to observed vector magnetograms. The decomposition employs the vector magnetograms alone, and does not require a model of the coronal configuration itself.

In spherical coordinates (θ, φ), the TFFF acquires the following form:

$$f\big|_{|\boldsymbol{x}|=1} = \int_0^{\pi} \mathrm{d}\tilde{\theta} \int_0^{2\pi} \mathrm{d}\tilde{\phi}\, \sin\tilde{\theta} \left(\boldsymbol{J}\cdot\hat{\boldsymbol{R}}\right) G_f \,,$$

$$G_f = -\ln\left[\Delta\left(1+\Delta/2\right)\right] \,,$$

where the radial component of the current density is assumed to be a given function of $\tilde{\theta}$ and $\tilde{\varphi}$. The Green's function G_f depends here only on

$$\Delta = \sqrt{2}\left(1-\hat{\boldsymbol{x}}\cdot\hat{\boldsymbol{R}}\right)^{1/2} \,,$$

which is the length of the chord connecting a source point $\mathbf{R}\hat{} = (\sin\tilde{\theta}\cos\tilde{\varphi}, \sin\tilde{\theta}\sin\tilde{\varphi}, \cos\tilde{\theta})$ and the observation point $\mathbf{x}\hat{} = (\sin\theta\cos\varphi, \sin\theta\sin\varphi, \cos\theta)$ at the photospheric boundary.

The surface term in the magnetogram-matching BSL represents the toroidal magnetic field. Applying this term to the photospheric boundary, we obtain

$$\boldsymbol{B}_T\big|_{|\boldsymbol{x}|=1} = \int_0^{\pi} \mathrm{d}\tilde{\theta} \int_0^{2\pi} \mathrm{d}\tilde{\phi}\, \sin\tilde{\theta} \left(\boldsymbol{J}\cdot\hat{\boldsymbol{R}}\right) \boldsymbol{G}_{B_T} \,,$$

$$\boldsymbol{G}_{B_T} = \frac{2\left(1+\Delta\right)}{\left(2+\Delta\right)\Delta^2}\left[\left(\hat{\boldsymbol{\phi}}\cdot\hat{\boldsymbol{R}}\right)\hat{\boldsymbol{\theta}} - \left(\hat{\boldsymbol{\theta}}\cdot\hat{\boldsymbol{R}}\right)\hat{\boldsymbol{\phi}}\right] \,,$$

where $\theta\hat{}$ and $\varphi\hat{}$ are the corresponding unit vectors of our spherical system of coordinates.

Thus, the TFFF and toroidal magnetic field are both determined at the photospheric boundary via the convolutions of the radial current density with the corresponding Green's functions.

Using the Green's function for the external Neumann problem of the Laplace equation in spherical geometry (Nemenman & Silbergleit 1999 (https://pubs.aip.org/aip/jap/article-abstract/86/1/614/489936/Explicit-Green-s-function-of-a-boundary-value?redirectedFrom=fulltexthttps://pubs.aip.org/aip/jap/article-

abstract/86/1/614/489936/Explicit-Green-s-function-of-a-boundary-value?redirectedFrom=fulltext), see their Eq. (8)), we have derived the following expression for the photospheric tangential component of the potential magnetic field:

$$\boldsymbol{B}_{Pt}\big|_{|\boldsymbol{x}|=1} = \int_0^{\pi} \mathrm{d}\tilde{\theta} \int_0^{2\pi} \mathrm{d}\tilde{\phi}\, \sin\tilde{\theta} \left(\boldsymbol{B}\cdot\hat{\boldsymbol{R}}\right) \boldsymbol{G}_{Pt}\,,$$

$$\boldsymbol{G}_{Pt} = -\frac{\left(\hat{\boldsymbol{\theta}}\cdot\hat{\boldsymbol{R}}\right)\hat{\boldsymbol{\theta}} + \left(\hat{\boldsymbol{\phi}}\cdot\hat{\boldsymbol{R}}\right)\hat{\boldsymbol{\phi}}}{\pi\left(2+\Delta\right)\Delta^3}\,,$$

where Δ is the same as above.

The TFFF iso-contours represent the integral lines of the toroidal magnetic field. Therefore, plotting these iso-contours is a natural way to visualize the toroidal magnetic field lines. By denoting the tangential field component of a measured photospheric vector magnetogram by $\mathbf{B}_t$ and subtracting from it the toroidal and tangential potential-field components, one obtains

$$\boldsymbol{B}_{Ic}\big|_{|\boldsymbol{x}|=1} = \left(\boldsymbol{B}_t - \boldsymbol{B}_T - \boldsymbol{B}_{Pt}\right)\big|_{|\boldsymbol{x}|=1}\,,$$

which is the field generated by all coronal current loops under the condition that their radial magnetic component vanishes at the photospheric boundary. Thus, the plotting of $\boldsymbol{B}_{Ic}$ can reveal the photospheric imprint of a closed coronal current field associated with a given vector magnetogram.

As a rule, MFRs reside above and along segments of the polarity inversion line (PIL). Therefore, if the total axial current in such an MFR differs from zero, or, in other words, this current is unneutralized, then the field $\boldsymbol{B}_{Ic}$ at the corresponding segment of the PIL allows one to establish this fact as well as to determine the direction of the current. As demonstrated in our examples, in combination with the TFFF iso-contours, this makes it possible to localize MFRs on the solar surface by using only magnetic data.

4. EXAMPLE 1: THE MODELED PRE-ERUPTIVE CONFIGURATION OF THE 2009 FEBRUARY 13 CME

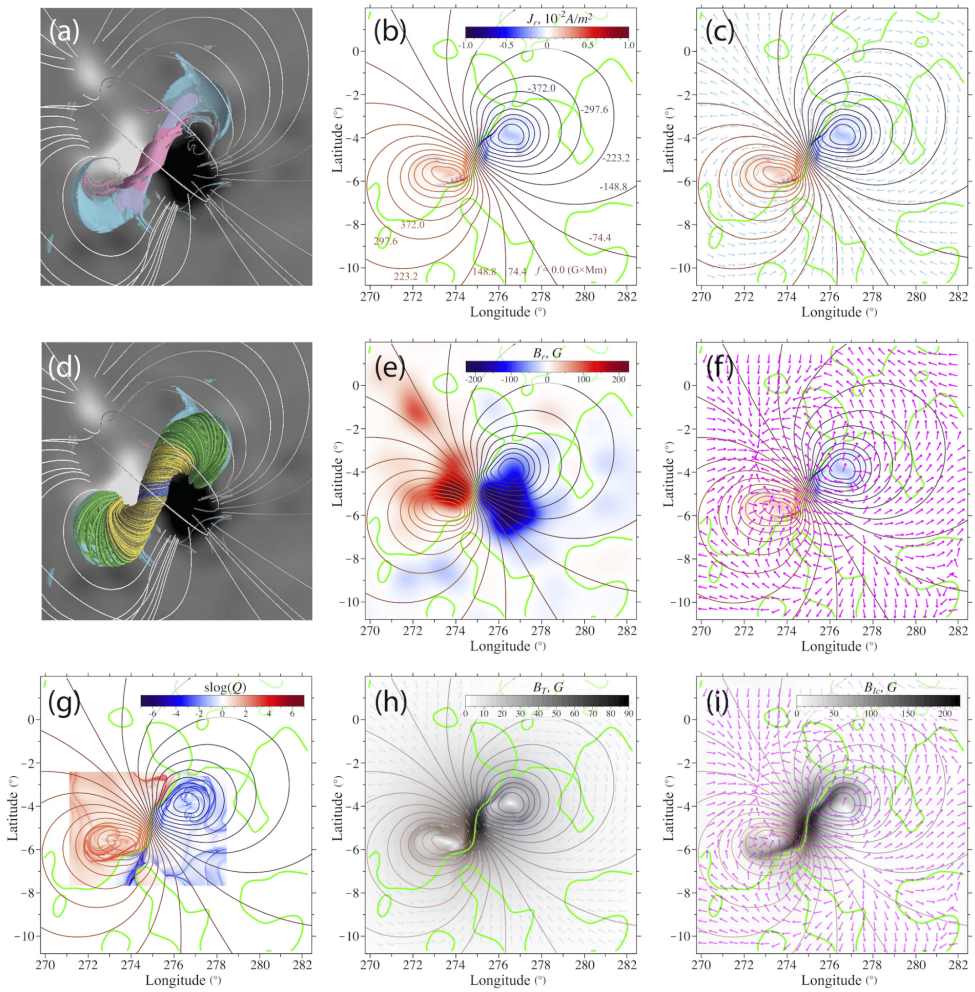

Figure 3.The photospheric magnetic field decomposition for the pre-eruptive configuration model of the 2009 February 13 CME: top view on the current (a) and field (d) structures (see in more details in Titov et al. 2021 (https://iopscience.iop.org/article/10.3847/1538-4365/abfe0f)); equidistant iso-contours of the TFFF are superimposed on the photospheric distributions of J_r (b), B_r (e), directional fields of $\boldsymbol{B}_T$ (c) (cyan arrows) and $\boldsymbol{B}_{lc}$ (f) (magenta), slog Q (log of the squashing factor Q signed with B_r) (g), B_T (h), and B_{lc} (i); thick green line is the polarity inversion line. The extremums of the TFFF well define the location of the MFR footprints.

Here is a decomposition of the photospheric magnetic field for a simple sigmoidal PEC model, which Titov et al. (2021) (https://iopscience.iop.org/article/10.3847/1538-4365/abfe0f) have previously described as Solution 1. They have found that the core of this PEC contains an MFR embedded in a sheared magnetic arcade such that the substantial part of its electrical current is concentrated in layers at the central part of the PEC. Panels (a) and (d) in Figure 3 provide the top views on the corresponding current and magnetic field structures of the core.

The photospheric distribution of the radial current density J_r is rather nontrivial. Panel (b) shows that this distribution combines relatively large spots of a low current density and narrow stripes of a high current density situated nearby and along the central part of the PIL. In contrast, the TFFF computed for this J_r–distribution has a

sufficiently simple pattern of equidistant iso-contours. They reveal two extremums located within the footprints of the MFR at the periphery of the magnetic flux spots (see panels (b)–(e)).

Using our theory described in Section 3, we have computed the photospheric magnetic components $\boldsymbol{B}_T$ and $\boldsymbol{B}_{Ic}$ whose directions in the region of interest are depicted at different points by cyan and magenta arrows in panels (c) and (f), respectively. They both match the direction of the modeled unneutralized MFR current that flows in the PEC from the positive to negative magnetic polarity. Indeed, first, as panel (c) shows, the directional field of $\boldsymbol{B}_T$ (cyan) forms a clockwise and counterclockwise vortex at the positive and negative magnetic polarity, respectively. Both vortices are centered around the footprints of the MFR. Second, panel (f) shows that at the PIL segment, along which the MFR resides, the directional field of $\boldsymbol{B}_{Ic}$ (magenta) is directed from the negative to positive magnetic polarity. It is evident that these directional properties of $\boldsymbol{B}_T$ and $\boldsymbol{B}_{Ic}$ are in agreement with what the curl right hand rule would provide us, given the known location and direction of the MFR current.

Panels (h) and (f) present the grayscaled distributions of $B_T \equiv |\boldsymbol{B}_T|$ and $B_{Ic} \equiv |\boldsymbol{B}_{Ic}|$, on top of which the corresponding directional fields and iso-contours of the TFFF are overlayed. As expected, the largest values of B_T and B_{Ic} are localized near the MFR by forming though somewhat different patterns. In particular, the B_T -distribution is largely concentrated at the central part of the PIL and, to a lesser extent, out from the PIL by encircling the MFR footprints. The B_{Ic}-distribution forms two J-like hooks adjacent to the same central part of the PIL. Therefore, the superposition of these two distributions would form a pattern of sigmoidal shape, which is a sort of photospheric imprint of the corresponding coronal magnetic structure.

Such a sigmoidal shape is also visible in the Q-map of the region of interest presented in panel (g) as the distribution of slog Q, which is essentially $\log_{10}$ of the squashing factor Q taken with the sign of the local B_r. The high-Q lines generally mark the footprints of quasiseparatrix layers (QSLs) formed by strongly divergent magnetic field lines. QSLs serve as interfaces between magnetic flux systems with different types of the field-line connectivity to the boundary. The meaning of the resulting, rather complex, Q-map for our PEC, was previously considered in detail by Titov et al. (2021) (https://iopscience.iop.org/article/10.3847/1538-4365/abfe0f). Here we just would like to point out that each magnetic polarity in this map contains a high-Q line of J-like shape that wraps around one of the two extremums of the TFFF. And, as explained above, these extremums reside at the centers of the MFR footprints.

Thus, the analyses of both the magnetic connectivity and TFFF allow one to identify approximately the same locations of the MFR footprints. However, the former approach requires the modeling of the whole PECs as well as the computation of the corresponding Q-maps, which are both technically nontrivial and numerically expensive procedures. In contrast, the latter approach relies only on a relatively simple convolution of the photospheric J_r-distributions, which can directly be determined from observed vector magnetograms without modeling the related PECs. It is also shown that the calculations using similar convolutions make it possible to find the magnetic field components $\boldsymbol{B}_{Ic}$ and $\boldsymbol{B}_T$, which are produced at the photosphere by the coronal current loops and their subphotospheric closure currents, respectively. In combination with the TFFF, these field components appear to provide valuable constraints on the modeling of MFR configurations.

5. EXAMPLE 2: THE PRE-ERUPTIVE CONFIGURATION AT THE ONSET OF THE 2011 OCTOBER 1 CME

From a practical point of view, it is important to check how our decomposition technique works with real vector magnetograms. For this purpose, let us apply it to the HMI SHARP cea vector magnetic data for the AR 11305 obtained approximately at 9:36 UT when the 2011 October 1 CME event started. Below we present the resulting decomposition for two different maps of the radial current density J_r.

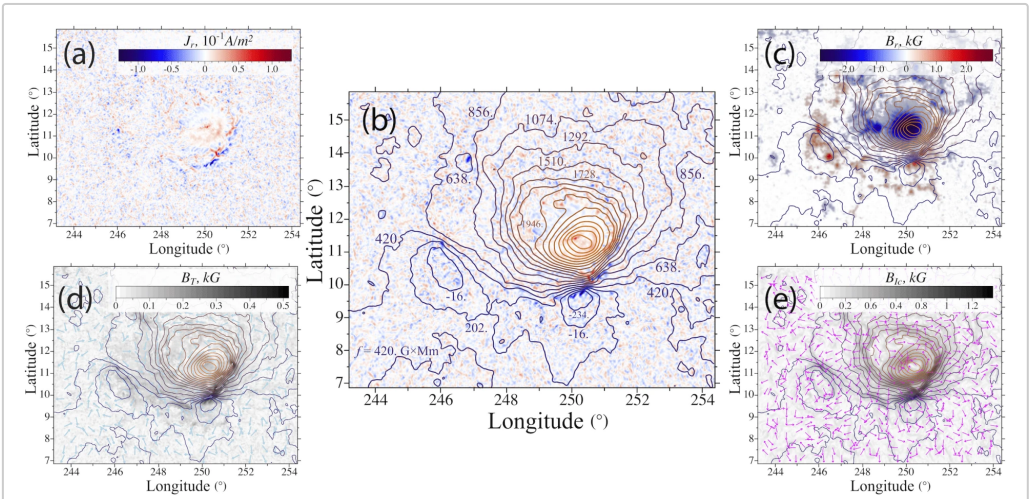

Figure 4. Decomposition of the vector magnetic data for the AR 11305 at 9:36 UT when the onset of the 2011 October 1 CME event occurred: the corresponding J_r-distribution (a) is used to calculate $\boldsymbol{B}_T$ and the TFFF whose equidistant iso-contours are superimposed on the corresponding distributions of J_r (b), B_r (c), B_T (d), and B_{Ic} (e). The directional fields of $\boldsymbol{B}_T$ (d) and $\boldsymbol{B}_{Ic}$ (e) are depicted by equidistant arrays of cyan and magenta arrows, respectively. The blue-red B_r -distribution is overlaid on the grayshaded areas of $B_r \geq 100$ G to bracket a segment of the polarity inversion line along which an MFR resides, being split into two parts and rooted at the TFFF extremums, one in the positive polarity and two in the negative one.

The first of these maps is derived by simply taking appropriate finite differences of the transverse components of the magnetogram. The decomposition based on this J_r -map is illustrated in Figure 4, where panel (a) demonstrates that the J_r-distribution is fragmented on numerous negative and positive spots of different strengths and sizes. Current spots of small strengths and sizes appear to be randomly distributed over the whole AR. In contrast, a signification fraction of current spots of larger strengths and sizes are aggregated in two unipolar necklace-like structures of opposite signs. According to panels (a), (b), and (c), these "necklaces" reside near the largest negative flux spot at different sides of the PIL and stretch along the PIL with some shift to each other.

In spite of such complex J_r-distribution, the corresponding TFFF has remarkably simple and coherent patterns of equidistant iso-contours, which clearly reveal the presence of three pronounced extremums of this function. One of them is a maximum located at the large negative flux spot, while the other two are minima located at two separate aggregations of small positive flux spots (see panel (c)). The above-mentioned randomness of weak-current spots manifests itself only in that the iso-contours of the TFFF have relatively uneven lines. Apparently, these properties of the TFFF are due to averaging of the contributions from different current spots in the AR. Indeed, the TFFF contributions from two neighboring current spots of similar strengths and sizes, but of opposite signs have to partially cancel each other in the linear superposition described in Section 3.

Panels (d) and (e) complement this information by showing gray shaded maps of B_T and B_{Ic} , which are overlaid with the corresponding directional fields and the same set of equidistant TFFF iso-contours. Panel (d) demonstrates that the toroidal field $\boldsymbol{B}_T$ is strongly sheared and localized at the "necklaces" of current spots. This fact is also reflected in the properties of the TFFF iso-contours, which tend to align with the "necklaces" and concentrate at them. Panel (e) shows that the field BIc has a similar localization in this region, but practically lacks

shear by traversing the iso-contours almost perpendicularly. This mutual orientation of the field $\boldsymbol{B}_{Ic}$ and iso-contours passing through the "necklaces" remains qualitatively the same all the way eastward along these iso-contours, i.e., when moving along them from one TFFF minimum to the other.

Similar to the case considered in Section 4, the described decomposition of the photospheric field can be interpreted as follows. The configuration under study contains two MFRs whose currents jointly start at the TFFF maximum (counterclockwise vortex) and separately end at one of the two TFFF minima (clockwise vortices). The direction of these currents is consistent with what follows from the curl right hand rule for the found directions of the vortex circulations and of the field $\boldsymbol{B}_{Ic}$ at the TFFF iso-contours passing through the current-spot "necklaces". As shown below, this interpretation also compares well with a numerical PEC model that we have developed earlier by using in the corresponding magnetic data only the photospheric B_r-distribution.

However, before doing this comparison, let us assess how sensitive our results are to the errors of magnetic field measurements. For this purpose, we have performed a similar decomposition of the same vector magnetic data by using a modified J_r-map, which is obtained by cleaning up the previous one from the current signals with a large uncertainty of the measurement. The uncertainty in the current for each pixel is propagated from provided transverse magnetic field error data. Active AR pixels and errors due to transverse field disambiguation are controlled by the bitmap and conf_disambig parameters (Hoeksema et al. 2014 (https://link.springer.com/article/10.1007/s11207-014-0516-8)), respectively. Pixels are kept in the cleaned map if they satisfy the following conditions: (1) They are classified as active pixels, (2) their current is greater than 1.5 times the corresponding error, and (3) they have a high confidence in the disambiguation algorithm. As a result of this cleaning procedure, most of randomly distributed weak-current spots have been removed from the data, while strong-current spots remained there by preserving, in particular, the above two necklace-like structures (panel (a) in Figure 5).

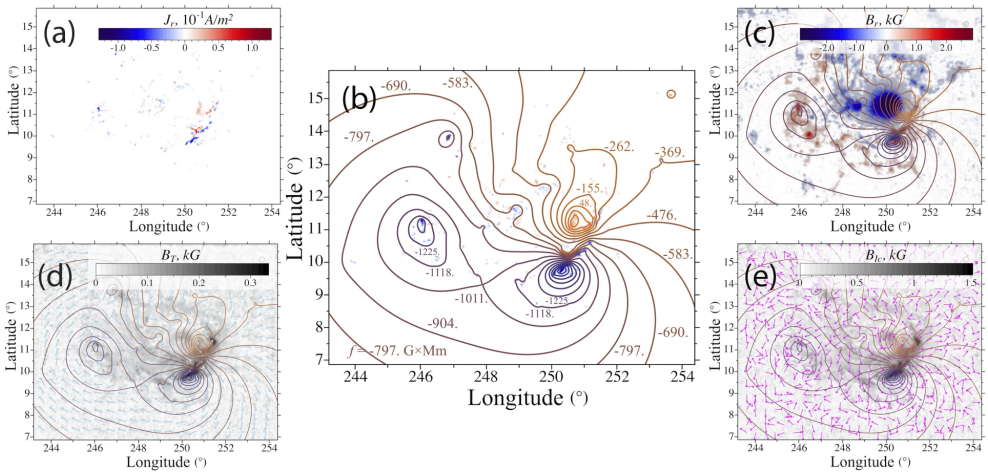

Figure 5. A similar set of panels as in Figure 4 for the same vector magnetogram, but for the convolutions with the J_r-distribution (a) where weak current spots with strengths below the estimated error of measurements have been removed.

Compared to the previous J_r-map, the new one provides the TFFF with much smoother iso-contours, because incoherent weak-current spots of the map do not contribute anymore to the resulting TFFF. Its equidistant iso-contours, however, demonstrate in panel (b) similar patterns, which reveal again two clockwise and one counterclockwise vortices at approximately the same locations as before. Note that these patterns now correspond to a different set of TFFF values, since the numerous weak-current spots have been excluded from the TFFF convolution. The exclusion from the convolution of the positive weak-current spots, grouped within the largest negative flux spot (see panels (b) and (c) in Figure 4), causes only a small shift of the counterclockwise vortex to the border of this flux spot (cf. panels (c) in Figures 4 and 5). Comparison of panels (d) and (e) in Figures 4 and 5 additionally confirms the similarity in the calculated fields $\boldsymbol{B}_T$ and $\boldsymbol{B}_{Ic}$ of the two decompositions.

Thus, in spite of significant differences between the original and cleaned J_r-maps, the vector-magnetogram decompositions based on these maps are qualitatively similar. In other words, the results of the latter decomposition equally well support what we already deduced from the former one, namely the conclusions on the

presence and locations of the two MFRs in the PEC under study. Therefore, such outcome of our decomposition procedure appears to be rather robust to the errors of measurements of the photospheric magnetic field. We think that this fact is related to a relative insensitivity of the TFFF to the details of the J_r-maps that are used for its calculation.

An additional evidence of the latter we have found by comparing the above decomposition results with those that refer to our β = 0 MHD modeling of the 2011 October 1 CME event. The results of the field decomposition for this model are shown in Figure 6, which presents similar panels as before for the moment when the modeled MFR starts to erupt.

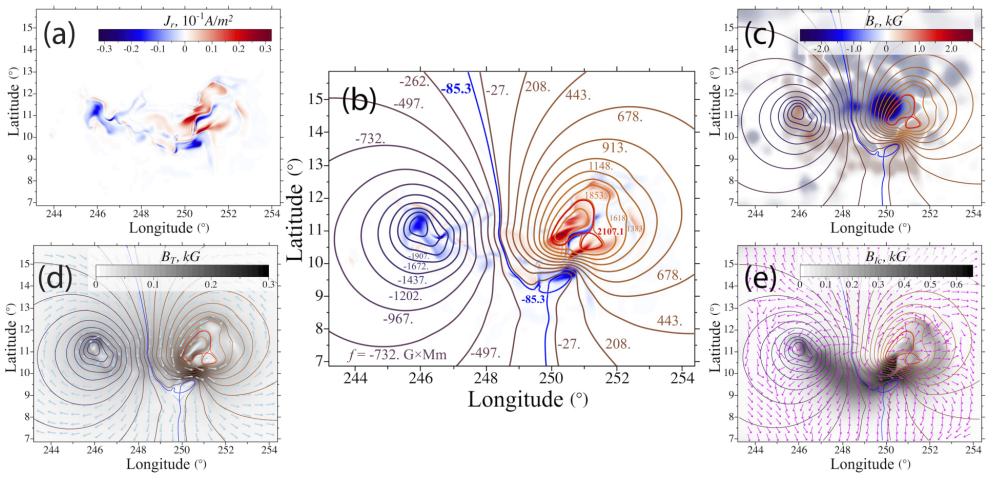

Figure 6. A similar set of panels as in Figures 4 and 5, but for the decomposition of the photospheric magnetic field in the pre-eruptive configuration of the 2011 October 1 CME event that was modeled via β = 0 MHD simulations. The MFR was constructed in this configuration by using RBSL and helicity-pumping methods under constraints that the observed photospheric B_r-distribution and corresponding coronal EUV images provide, as described in (Titov et al. 2018 (https://iopscience.iop.org/article/10.3847/2041-8213/aaa3da); Titov et al. 2021 (https://iopscience.iop.org/article/10.3847/1538-4365/abfe0f); Titov et al. 2022 (https://iopscience.iop.org/article/10.3847/1538-4357/ac874e)).

Note that this model was constructed long before the development of our decomposition technique. First steps of this model construction, using our RBSL method to build and optimize an MFR in the PEC under study, was described in (Titov et al. 2018 (https://iopscience.iop.org/article/10.3847/2041-8213/aaa3da); Titov et al. 2021 (https://iopscience.iop.org/article/10.3847/1538-4365/abfe0f)). Then the constructed PEC was energized toward an eruption by applying our helicity pumping method (Titov et al. 2022 (https://iopscience.iop.org/article/10.3847/1538-4357/ac874e)).

It is important for the comparison with the above results that the modeled PEC was constrained by using only the observed photospheric B_r-distribution and the corresponding EUV images of the AR. These images were used, in particular, to identify the locations of the modeled MFR footprints, which were needed, in turn, to construct the MFR with the RBSL method. It is evident from the comparison of Figures 4–6 that the TFFF extremums or vortices derived for our modeled and observed vector magnetic data match well enough. Moreover, during the MHD relaxation of our initial approximate equilibrium, the RBSL MFR splits to give birth to a new MFR of a shorter length whose footprint emerged in the positive magnetic polarity very close to what the decomposition of the observed vector magnetogram predicted.

6. SUMMARY

1. We have derived the magnetogram-matching Biot-Savart law for the coronal current that can be either concentrated at a given line or distributed in the volume. By definition, this law determines the magnetic field produced by the current under the condition that its radial magnetic component vanishes at the photospheric surface.
2. By applying this law to the subphotospheric closure currents, we have shown that they produce the toroidal magnetic field whose distribution is in general determined via the surface integral of the photospheric radial current density.
3. By using the radial components of the current density and magnetic field as input data, we have proposed a new method for decomposing the photospheric vector magnetic data into the following three components: (1) the fields produced by coronal current loops as well as (2) their subphotospheric closure currents under the condition that their resulting radial components identically vanish, and (3) the tangential potential magnetic field that is determined by the radial magnetic component and is generated by subphotospheric currents not reaching the photospheric surface.
4. Our field decomposition makes it possible to reveal the location of magnetic flux ropes in projection to the photospheric surface, and particularly their footprint locations. This provides valuable constraints on the modeling of pre-eruptive magnetic configurations as well as important information for the analysis of observations.
5. Our field decomposition is similar to the one recently described by Schuck et al. (2022) (https://iopscience.iop.org/article/10.3847/1538-4357/ac739a), but may lead to a somewhat different physical interpretation. In particular, in our approach the coronal current loops do not affect the radial magnetic component at the photospheric boundary. Because our magnetogram-matching BSL implicitly takes into account the back reaction from the dense photospheric and subphotospheric layers that suppress a penetration of this component from the corona into these layers.

TRANSCRIPT

ABSTRACT

We have derived a new form of the Biot-Savart law that allows one to calculate the coronal magnetic field generated by a closed line current under the condition that its radial component vanishes at the photospheric boundary. By investigating the field contributions from the coronal and sub-photospheric parts of the current path, C and C*, respectively, we have proven that the field produced at the C*-path depends only on its foot points, but not on its shape. We have found an exact analytical expression for this field and proven its toroidal nature. A part of the expression related to one of the foot points represents the Green's function for calculating more general toroidal fields determined by arbitrary boundary distributions of the radial current density.

The results we have obtained should be useful for constructing pre-eruptive magnetic configurations (PECs) in the following two ways. First, PECs can often be modeled by thin magnetic flux ropes (MFRs) whose fields are superimposed on ambient potential fields. The exterior field of the MFR is well approximated in these cases by the potential field of a curved line current. The latter field is conveniently described by our modified Biot-Savart law, since its superposition with the ambient field does not change the radial component at the boundary. Second, the Green's function we have calculated for the toroidal field enables one to reveal individual contributions of the sub-photospheric and coronal currents to a given vector magnetogram. On this basis, it becomes possible to approximately identify the locations of the MFR footprints at the magnetogram and verify whether the MFR body follows the polarity inversion line. This provides important, purely magnetic, constraints for modeling the corresponding PECs.

This research was supported by the NASA's HTMS and HSR programs, and the NSF's PREEVENTS and Solar-Terrestrial programs.

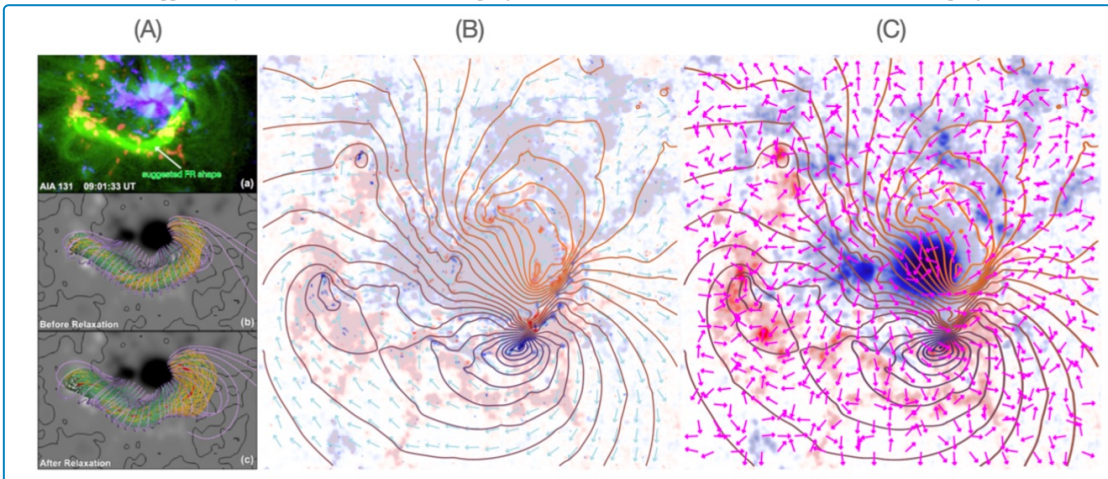

Figure 1. 2011 October 1 CME event: (A) the RBSL MFR model (Titov et al. 2018; Titov et al. 2021) of the PEC compared to the AIA 131 Å image of the active region at the onset of the eruption, (B) iso-contours of the toroidal flux function superimposed on the measured photospheric j_r-distribution and the directional toroidal field (cyan arrows), (C) the same iso-contours superimposed on the observed photospheric B_r-distribution and directional field (magenta arrows) generated by the coronal currents under the condition that the photospheric B_r component vanishes. The bluish and reddish shadings on panels (B) and (C) designate the areas of negative and positive polarities, respectively, with $|B_r| \geq 100$ G. Note that the locations of the extremums of the toroidal flux function and the MFR footprints match one another. Also the directions of the magenta arrows at the polarity inversion line are consistent with the direction of the MFR current out from the leading negative flux spot.

(https://agu.confex.com/data/abstract/agu/fm23/5/8/Paper_1304285_abstract_1183009_0.jpg)

REFERENCES

Axler, S. J., Bourdon, P., & Ramey, W. 2001, Graduate texts in mathematics, Vol. 137, Harmonic function theory (Berlin: Springer, 259 p.)

Hoeksema, J. T., Liu, Y., Hayashi, K., et al. 2014, SoPh, 289, 3483, doi: 10.1007/s11207-014-0516-8 (https://link.springer.com/article/10.1007/s11207-014-0516-8)

Nemenman, I. M., & Silbergleit, A. S. 1999, Journal of Applied Physics, 86, 614, doi: 10.1063/1.370775 (https://pubs.aip.org/aip/jap/article-abstract/86/1/614/489936/Explicit-Green-s-function-of-a-boundary-value?redirectedFrom=fulltext)

Schuck, P. W., Linton, M. G., Knizhnik, K. J., & Leake, J. E. 2022, ApJ, 936, 94, doi: 10.3847/1538-4357/ac739a (https://iopscience.iop.org/article/10.3847/1538-4357/ac739a)

Titov, V. S., Downs, C., Mikic´, Z., et al. 2018, ApJL, 852, L21. doi: 10.3847/2041-8213/aaa3da (https://iopscience.iop.org/article/10.3847/2041-8213/aaa3da)

Titov, V. S., Downs, C., To¨ro´k, T., & Linker, J. A. 2022, ApJ, 936, 121, doi: 10.3847/1538-4357/ac874e (https://iopscience.iop.org/article/10.3847/1538-4357/ac874e)

Titov, V. S., Downs, C., To¨ro´k, T., et al. 2021, ApJS, 255, 9, doi: 10.3847/1538-4365/abfe0f (https://iopscience.iop.org/article/10.3847/1538-4365/abfe0f)

EVALUATIONS

#	Average Score
There are currently no completed evaluations for this presentation	